



Microstructure evolution during near- T_g annealing and its effect on shear banding in model alloys

Meng-Hao Yang ^{1,2} Bei Cai,³ Yang Sun ^{1,2} Feng Zhang,^{1,2,*} Yi-Fan Wang,⁴ Cai-Zhuang Wang,^{1,2} and Kai-Ming Ho^{1,2}

¹*Ames Laboratory, United States Department of Energy, Ames, Iowa 50011, USA*

²*Department of Physics, Iowa State University, Ames, Iowa 50011, USA*

³*Key Laboratory of Advanced Materials (MOE), School of Materials Science and Engineering, Tsinghua University, Beijing 100084, China*

⁴*Systems Engineering Research Institute of China State Shipbuilding Corporation Limited*



(Received 21 August 2019; published 9 December 2019)

By performing extensive molecular dynamics simulations, we investigate the deformation behavior in $\text{Al}_{90}\text{Sm}_{10}$ and $\text{Cu}_{64.5}\text{Zr}_{35.5}$ alloys after elongated isothermal annealing in the vicinity of the glass-transition temperature (T_g). Different microstructural response to the annealing process was observed: $\text{Al}_{90}\text{Sm}_{10}$ maintains the glassy structure with improved energetic stability, enhanced short-range order (SRO), and a more pronounced spatial network that extends beyond the first atomic shell, while $\text{Cu}_{64.5}\text{Zr}_{35.5}$ forms nanocrystalline Laves Cu_2Zr phases. Shear banding occurs in both annealed systems under shear loading. For $\text{Al}_{90}\text{Sm}_{10}$, the spatial network formed by the local clusters characterizing the SRO of the system is significantly weakened but remains appreciable in the shear band. In contrast, the crystalline ordering in the $\text{Cu}_{64.5}\text{Zr}_{35.5}$ is completely destroyed during shear banding. Consequently, while displaying higher yield strength, the annealed $\text{Cu}_{64.5}\text{Zr}_{35.5}$ sample appears to be less ductile. By carefully examining the effect of microstructures on the structural ordering in the shear band and the consequent mechanical response, our work contributes to a better understanding of the deformation mechanism of amorphous alloys as compared with that in crystalline materials.

DOI: [10.1103/PhysRevMaterials.3.125602](https://doi.org/10.1103/PhysRevMaterials.3.125602)

I. INTRODUCTION

Metallic glasses (MGs) are a class of alloys with non-crystalline atomic structures and have attracted wide attention during the past decades. They are technologically important because of their excellent mechanical properties as promising engineering structural materials [1–4]. However, the deformation mechanism of MGs under mechanical loading is not fully understood yet. This is in contrast with their crystalline counterparts. Owing to the underlying periodic lattice, the mechanical response in crystalline materials can be well explained on the basis of fundamental lattice defects, such as dislocations, twinning, and domain boundaries [5–7]. For MGs, while it is generally accepted that shear banding is the dominant mode for plastic deformation [8], details on how the shear band forms and propagates remain unclear.

These questions are hard to address, partially because it is challenging to probe the shear-band structure at the atomic scale in experiments. For this reason, molecular dynamics (MD) has become the main theoretical method complementary to experimental tools [9–11]. On the other hand, MD also faces a significant limitation; that is, it can only access relatively short timescales compared with experiments [12]. Recently, it was proposed that annealing near the glass-transition temperature (T_g) can accelerate the dynamics and effectively reduce the gap between experimental and computational timescales [13–16]. For example, when applied on $\text{Cu}_{64.5}\text{Zr}_{35.5}$ and $\text{Al}_{90}\text{Sm}_{10}$ alloys, near- T_g annealing can pro-

duce effective cooling rates on the order of 10^7 K/s [17,18], which is approaching the experimental limit of $\sim 10^6$ K/s.

In the present work, we reexamined near- T_g annealing in much larger samples (containing more than 3×10^5 atoms) of the typical glass-forming systems $\text{Al}_{90}\text{Sm}_{10}$ and $\text{Cu}_{64.5}\text{Zr}_{35.5}$, for the purpose of studying subsequent deformation behaviors under shear loading. During the elongated annealing, $\text{Al}_{90}\text{Sm}_{10}$ maintains the glassy structure, while the $\text{Cu}_{64.5}\text{Zr}_{35.5}$ alloy develops nanocrystalline Laves phases, which is consistent with several previous studies [19,20]. Meanwhile, $\text{Cu}_{64.5}\text{Zr}_{35.5}$ displays higher shear strength but lower ductility than $\text{Al}_{90}\text{Sm}_{10}$. We demonstrated that these differences in mechanical properties can be well tied to the different structural ordering in shear bands. This comparative study of shear banding in two seemingly disordered systems with distinctive nanoscale structures provides detailed insights into understanding the deformation mechanism in MGs, as compared with crystalline structures.

II. METHODS AND MODELS

We chose two prototypical MG-forming systems, $\text{Al}_{90}\text{Sm}_{10}$ and $\text{Cu}_{64.5}\text{Zr}_{35.5}$, in the present work. Classical potentials in the Finnis-Sinclair form [21] were used for energy and force calculations for these two alloys [22,23]. MD simulations under NPT (constant numbers of atoms, pressure, and temperature) ensemble were performed using the GPU-accelerated LAMMPS code [24,25], with a time step of 2.5 fs. The initial $\text{Al}_{90}\text{Sm}_{10}$ and $\text{Cu}_{64.5}\text{Zr}_{35.5}$ glass samples, containing 345,600 atoms with box sizes $254 \times 51 \times 507 \text{ \AA}^3$ and $240 \times 48 \times 479 \text{ \AA}^3$, respectively,

*Corresponding author: fzhang@ameslab.gov

were prepared by quenching a liquid from 2000 to 300 K at a rate of 10^{10} K/s and are called “as-quenched” samples hereafter. In addition, two other samples were prepared for each system by quenching the liquid to an intermediate temperature T_a first, followed by isothermal annealing at T_a for 100 and 300 ns, and finally quenching to 300 K. All quenching rates were kept the same, i.e., 10^{10} K/s. T_a was set to 655 and 780 K, which are close to the corresponding glass-transition temperatures 693 [23,26,27] and 750 K [22], for $\text{Al}_{90}\text{Sm}_{10}$ and $\text{Cu}_{64.5}\text{Zr}_{35.5}$, respectively.

All samples were then relaxed to the inherent structures at zero pressure by minimizing the potential energy with a damped dynamics method [28]. Afterwards, the model MGs were heated to a cryogenic temperature of 50 K and were compressed along the Z direction with a constant deformation rate of $2.5 \times 10^7 \text{ s}^{-1}$ until the strain reached 10%. Periodic boundary conditions were only applied in the Y and Z directions, and free surfaces were adopted in the X direction to adapt the shear offset. To quantify the atomic-scale deformation, the nonaffine displacement D_{\min}^2 [29] is used, which has been widely used as an excellent indicator of local irreversible deformation. After obtaining the atomic positions and subsequent displacements, the local strain tensor of the neighborhood of any specific atom can be calculated as

$$D^2(t) = \sum_n \sum_i \left(r_n^i(t) - r_0^i(t) - \sum_j (\delta_{ij} + \varepsilon_{ij}) [r_n^j(0) - r_0^j(0)] \right)^2, \quad (1)$$

where $r_n^i(t)$ is the i th component of the position of the n th atom at time t , and the index n runs over the atoms within the interaction range of the reference atom. The uniform strain ε_{ij} to minimize D^2 can be calculated by

$$X_{ij} = \sum_n [r_n^i(t) - r_0^i(t)] [r_n^j(0) - r_0^j(0)], \quad (2)$$

$$Y_{ij} = \sum_n [r_n^i(0) - r_0^i(0)] [r_n^j(0) - r_0^j(0)], \quad (3)$$

$$\varepsilon_{ij} = \sum_k X_{ik} Y_{jk}^{-1} - \delta_{ij}. \quad (4)$$

The minimum of $D^2(t)$ during the time t is the local deviation from affine deformation, which is marked as D_{\min}^2 and used to divide the shear band (SB) and matrix regions.

To characterize the evolution of structural order during the annealing and loading process, we applied the cluster alignment method [30,31] to quantitatively determine the similarity between local clusters in the samples and various templates. After alignment, an alignment score is defined as

$$f = \min_{0.80 \leq \alpha \leq 1.2} \left(\frac{1}{N} \sum_{i=1}^N \frac{(\vec{r}_{ic} - \alpha \vec{r}_{it})^2}{(\alpha \vec{r}_{it})^2} \right)^{1/2}, \quad (5)$$

where N is the number of atoms within the first shell, and \vec{r}_{ic} and \vec{r}_{it} refer to the atomic positions in the cluster and the template, respectively. The coefficient α in the range from 0.8 to 1.2 is used to adapt the template's bond length to reach

a maximal overlap between the cluster and the template. A smaller alignment score means a higher structure similarity for the given cluster.

To describe the dominant short-range order in the simulated samples, the aligned clusters against the same template were superposed by overlapping their center atoms [32]. A continuous atomic density of the superposed clusters in a three-dimensional (3D) view can be determined by a Gaussian-smearing scheme:

$$D(\vec{r}) = \frac{1}{m} \times \sum_{i=1}^{m \times n} \left(\frac{\beta}{\pi} \right)^{3/2} e^{-\beta \times (\vec{r} - \vec{r}_i)^2}, \quad (6)$$

where \vec{r}_i is the atomic coordinate for each particle i , β is a constant scaling factor, and m and n are the number of superposed clusters and the number of atoms per cluster, respectively.

III. RESULTS AND DISCUSSIONS

A. Deformation behavior and shear transformation zone

The stress-strain curves for as-quenched and annealed $\text{Al}_{90}\text{Sm}_{10}$ and $\text{Cu}_{64.5}\text{Zr}_{35.5}$ alloys are illustrated in Fig. 1. During the initial elastic stage, the stress increases linearly with the strain; after that, plastic deformation emerges as the stress deviates from the linear dependence on the strain. There exist two characteristic stresses, τ_y and τ_s , employed to distinguish two different structural states of model alloys [33–35]. The strength τ_y can be used to motivate the subsequent apparent plastic flow. After the stress reaches the maximum value (τ_y), the stress of the model alloy experiences an abrupt decrease in strength. The speed at which the stress decreases can be used to characterize the ductility (or brittleness) of the sample. As the shear strain increases, the structural disordered regions become obvious, and the alloy is softened and becomes easier to be cut and shaped. When the strain approaches around 0.06, the shear band can propagate, and the stress would enter a steady-state (τ_s) flow. The strength difference between τ_y and τ_s , i.e., $\Delta\tau = \tau_y - \tau_s$, reflects the degree of softening upon rejuvenation deviated from the original structures [36–38]. For the $\text{Al}_{90}\text{Sm}_{10}$ alloy, the stress drop $\Delta\tau$ gradually increases with the annealing time. Such a trend is more noticeable for the $\text{Cu}_{64.5}\text{Zr}_{35.5}$ alloy. More interestingly, the $\text{Cu}_{64.5}\text{Zr}_{35.5}$ sample annealed for 300 ns undergoes the sharpest drop in stress after reaching τ_y , indicating that this sample has lower ductility than other $\text{Cu}_{64.5}\text{Zr}_{35.5}$ or $\text{Al}_{90}\text{Sm}_{10}$ samples. These facts suggest that possibly different responses in microstructure to the annealing process occurred in these two systems.

The configurational potential energy (PE) [39,40] has been reported to successfully characterize the relationship between strain localization and the microstructure. The average potential energy of two model alloys as a function of strain is illustrated in the insets of Fig. 1. Initially, the potential energy increases gradually with straining as the deformation energy is stored in the alloy; then, a sudden drop occurs that coincides with the similar drop in the stress-strain curve. With the annealing time increasing, the average potential energy of the two model alloys decreases, indicating the stabilization effect of the annealing process. Obviously, the potential energy drop of the $\text{Cu}_{64.5}\text{Zr}_{35.5}$ alloy is much more significant than that of

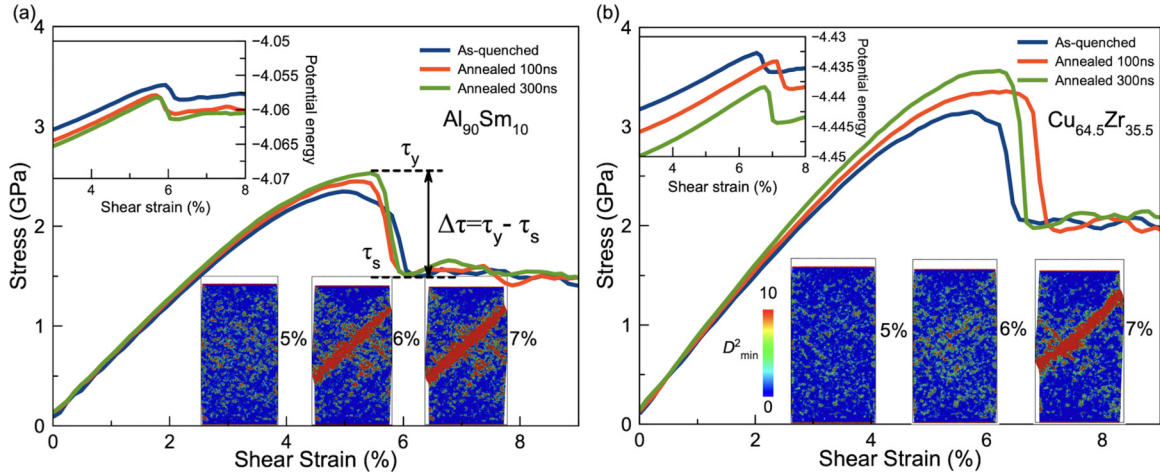


FIG. 1. Stress-strain curve for as-quenched and annealed (a) $\text{Al}_{90}\text{Sm}_{10}$ and (b) $\text{Cu}_{64.5}\text{Zr}_{35.5}$ model alloys, respectively. The inset shows the potential energy curve of the simulated samples as a function of shear strain. It can be seen that the shear band and matrix regions of the typical samples were characterized by the minimum nonaffine displacement D_{\min}^2 .

the $\text{Al}_{90}\text{Sm}_{10}$ alloy, again indicating different microstructures of these two samples after annealing. Also included in Fig. 1 are the atomic structures at different deformation stages with the atoms colored according to the nonaffine displacements D_{\min}^2 . One can see how the SB of samples was initiated and developed, and the SB direction was parallel to a principle axis of the shear stress [29]. This means that the final fracture of alloys results from the localization and propagation of shear transformation zones, and the plasticity of model alloys was relatively low. The stored PE can be released into the narrow shear band after the model alloys reach a steady-state flow.

B. Structure evolution under annealing

In order to understand the different stress-strain response in the two systems, we first examine the structural evolution of load-free model alloys with different annealing times. As shown in Fig. 2(a), while the pair-correlation function $g(r)$ for the as-quenched and annealed $\text{Al}_{90}\text{Sm}_{10}$ alloys largely overlaps, a slight enhancement on the second peak with increasing annealing time is still observable. On the other hand, there exists a more pronounced difference in the $g(r)$ curves for the as-quenched and annealed $\text{Cu}_{64.5}\text{Zr}_{35.5}$ alloys: as the annealing time increases, the first peak significantly drops, a side shoulder before the second major peak in the range from 4.0 to 5.0 Å is developing into a full peak, and the valley

between 5.0 and 5.5 Å also significantly decreases. These results suggest that, during annealing, $\text{Cu}_{64.5}\text{Zr}_{35.5}$ undergoes a more notable structural change than $\text{Al}_{90}\text{Sm}_{10}$ in both short-range order (SRO) and medium-range order (MRO).

Cluster alignment analysis was also performed to quantitatively characterize the dominant local order motifs in the simulated alloys. Clusters extracted from the $\text{Al}_{90}\text{Sm}_{10}$ sample were aligned against an Al-centered icosahedron and a Sm-centered “3661” polyhedron, which have been established as typical motifs in this system [17]. For $\text{Cu}_{64.5}\text{Zr}_{35.5}$, a Cu-centered icosahedron and a Zr-centered Frank-Kasper Z16 were chosen as templates [41]. As shown in Fig. 3, while there is some increase of population in the low-score (high-similarity) region, the overall distributions of the alignment score for the as-quenched and annealed $\text{Al}_{90}\text{Sm}_{10}$

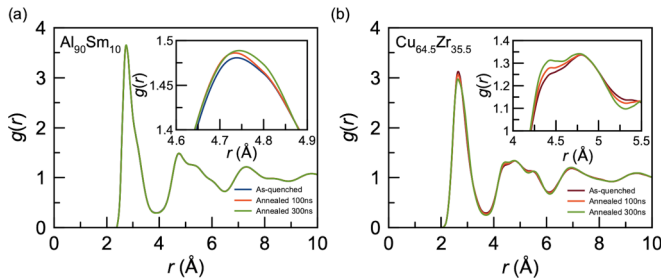


FIG. 2. Total pair correlation function of as-quenched and annealed (a) $\text{Al}_{90}\text{Sm}_{10}$ and (b) $\text{Cu}_{64.5}\text{Zr}_{35.5}$ model alloys, respectively. The insets zoom in on certain sections to highlight the difference.

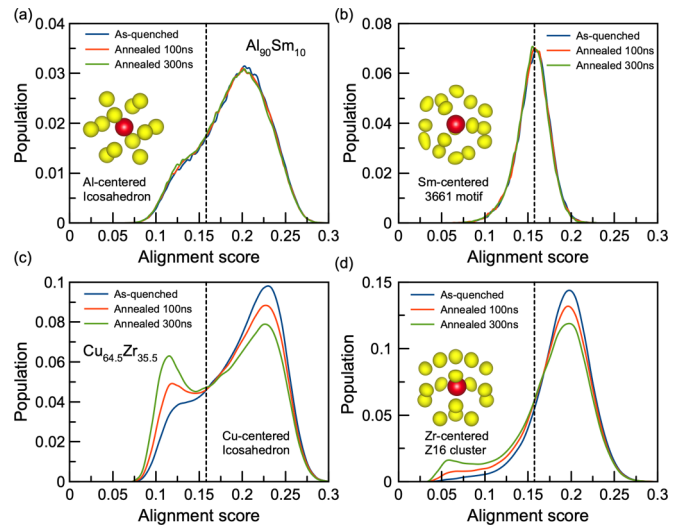


FIG. 3. The alignment score distribution for (a) Al-centered and (b) Sm-centered clusters of the simulated $\text{Al}_{90}\text{Sm}_{10}$ model alloys, and the corresponding score distribution of (c) Cu-centered and (d) Zr-centered clusters of $\text{Cu}_{64.5}\text{Zr}_{35.5}$ model alloys. A cutoff alignment score of 0.16 was used to calculate the fractions of clusters.

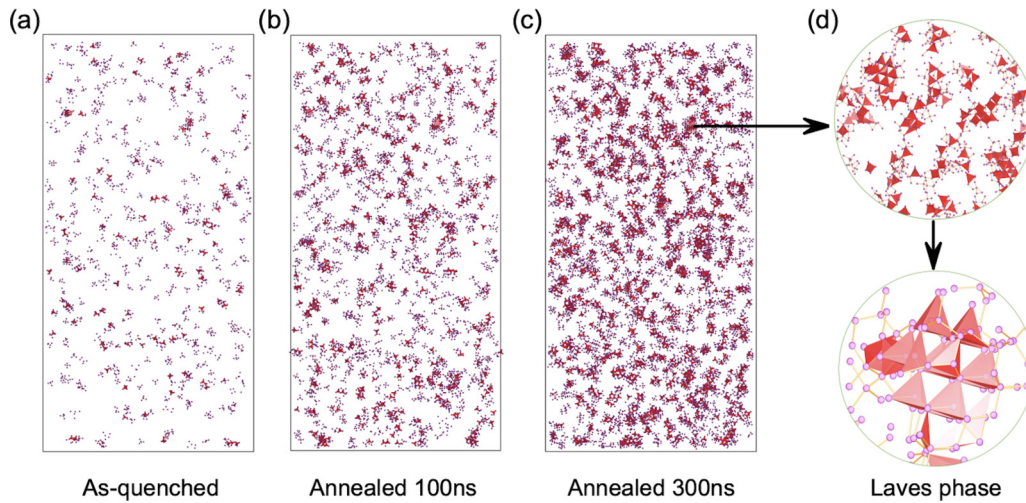


FIG. 4. (a)–(c) Snapshots of TC Zr atoms in as-quenched and annealed $\text{Cu}_{64.5}\text{Zr}_{35.5}$ model alloys. (d) Zoom-in of a portion of (c) to show the typical tetrahedral network for the Laves Cu_2Zr phase.

alloys remain largely overlapping. In summary, one can clearly observe a strong enhancement of the first peak for the alignment distributions of both Cu-centered and Zr-centered clusters with increasing annealing time.

C. Nanocrystalline phase formation in $\text{Cu}_{64.5}\text{Zr}_{35.5}$

As can be seen in the above sections, the changes in the potential energy (see inset of Fig. 1), $g(r)$ (see Fig. 2), and the SRO (see Fig. 3) in the $\text{Cu}_{64.5}\text{Zr}_{35.5}$ sample all exceed the range that can be explained by glass aging under near- T_g annealing [17,18,42]. This suggests that nanocrystallization might have occurred, similar to what has been reported for this system under relatively slow cooling [43]. The possible crystal structure involved in crystallization is a Laves-phase Cu_2Zr with the prototype MgCu_2 [44]. The Cu_2Zr compound was first suggested in a study of the phase diagram of a Cu-Zr system [45]. Afterwards, the formation of the Cu_2Zr compound was identified and analyzed in terms of thermodynamic properties using the Knudsen method of mass spectrometry [46,47]. Later, *ab initio* total-energy [48,49] as well as MD [50] calculations confirmed that Cu_2Zr is a metastable phase at low temperature.

In the Laves Cu_2Zr phase, Zr atoms form a diamondlike tetrahedral network. In Fig. 4, we show the tetrahedrally coordinated (TC) Zr atoms identified by the cluster-alignment method in samples with different annealing time. The increasing density of TC Zr atoms clearly shows the amount of crystalline Cu_2Zr phase during annealing.

Figure 5(a) shows the change of TC Zr atoms with the shear strain. For the as-quenched sample, no crystallization occurs, and the TC Zr atoms are randomly distributed in the sample, possibly serving as precursors for nucleation [see Fig. 4(a)]. The total number is also weakly dependent on the strain. On the other hand, for the two annealed samples, the number of TC Zr atoms significantly drops as the shear strain increases, since more and more tetrahedral clusters with increasing deformations will align negatively against an ideal tetrahedron template. As shown in Fig. 5(b), essentially no TC Zr atoms can be found in the SB, indicating the crystalline order is completely destroyed in the SB, which is also the reason that the amount of TC Zr atoms levels off in the steady-state zone for the annealed samples [see Fig. 6(a)]. This also indicates that the relatively larger strain scales will disturb the formation of TC clusters [51].

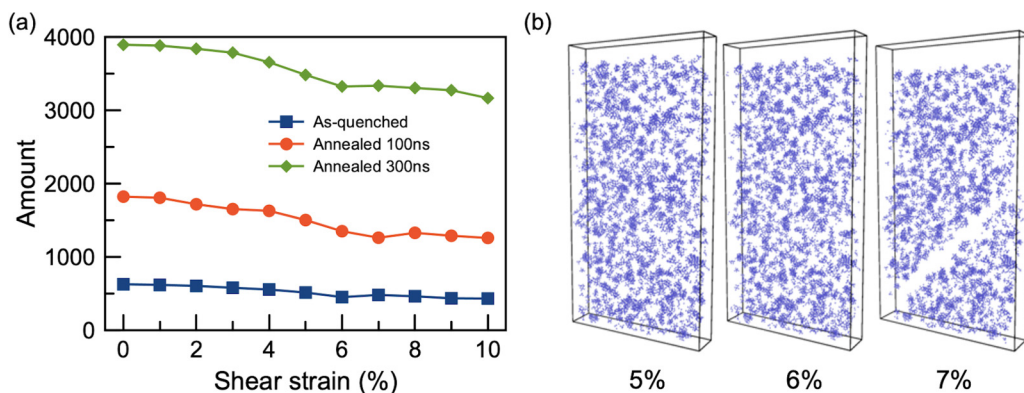


FIG. 5. (a) The number of TC Zr atoms as a function of shear strain in the $\text{Cu}_{64.5}\text{Zr}_{35.5}$ alloy annealed for 300 ns. (b) Snapshots of TC Zr atoms at several shear strains in the $\text{Cu}_{64.5}\text{Zr}_{35.5}$ alloy annealed for 300 ns.

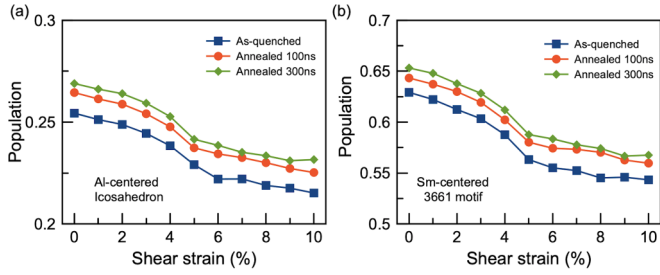


FIG. 6. Population of (a) Al-centered icosahedral and (b) Sm-centered “3661” clusters of the $\text{Al}_{90}\text{Sm}_{10}$ model alloys as a function of the shear strain.

D. Fractal cluster network in $\text{Al}_{90}\text{Sm}_{10}$

Unlike $\text{Cu}_{64.5}\text{Zr}_{35.5}$, the effects of annealing on $\text{Al}_{90}\text{Sm}_{10}$ samples can be well explained by the aging effect in glassy structures, which is consistent with our previous study [52]. Here, we examine how the structural order responds to the external shear loading. Figure 6(a) shows that in all three $\text{Al}_{90}\text{Sm}_{10}$ samples, the fraction of Al-centered icosahedral and Sm-centered “3661” clusters decreases with the shear strain in the elastic region. In the steady-state zone ($\tau \approx \tau_s$), on the other hand, the dependence of the fraction of these clusters on the strain is notably weakened.

To show how the shear band and the surrounding matrix respond differently to the shear strain, we first separate the shear band and the matrix in the sample based on a cutoff value of D_{\min}^2 : the regions with D_{\min}^2 greater than 10 are called metallic glass matrices, while the remaining are the strained regions. Figures 7(b) and 7(c) show the distribution of alignment score for Al- and Sm-centered clusters, respectively. For both Al-centered icosahedral and Sm-centered “3661” motifs in Figs. 7(b) and 7(c), the alignment score of the matrix region is smaller than that of the shear-band region as the alignment distribution of the shear band moves to the right, suggesting that the matrix is more ordered. On the other hand, the SRO

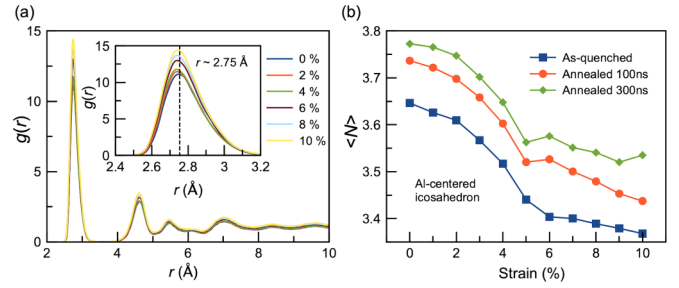


FIG. 8. (a) The pair-correlation function of the Al atoms that form centers of icosahedra clusters in the $\text{Al}_{90}\text{Sm}_{10}$ sample annealed for 300 ns under different shear strains. (b) The average coordination number $\langle N \rangle$ for the Al-centered icosahedral network in this sample.

surrounding both Al and Sm atoms in the shear band is still appreciable.

Next, we extend beyond the first atomic shell by examining the spatial network of the dominant atomic clusters in the $\text{Al}_{90}\text{Sm}_{10}$ model alloy. In particular, we analyze how the Al-centered icosahedral clusters develop into the spatial network in glassy samples. The pair-correlation functions of the centers of the icosahedral clusters are shown in Fig. 8(a), along with the inset of the first peak positions under different shear strains. One can see from the inset of Fig. 8(a) that the strong peaks are almost located at ~ 2.75 Å, which is contributed by the center atoms forming nearest-neighboring pairs. This clearly indicates that the icosahedral clusters form an extensive interpenetrating network, and such a network does extend to the shear-band region.

One parameter to describe the degree of connectivity of the network is the average coordination number $\langle N \rangle$, defined as the number of nearest-neighboring pairs that each icosahedral center forms with other icosahedral centers [53,54]. Based on a cutoff distance of 3.2 Å, at which the first peak of $g(r)$ vanishes [see Fig. 8(a)], we calculated $\langle N \rangle$ and plotted it as a function of the shear strain in Fig. 8(b). At zero strain, $\langle N \rangle$ increases with the annealing time, indicating enhanced

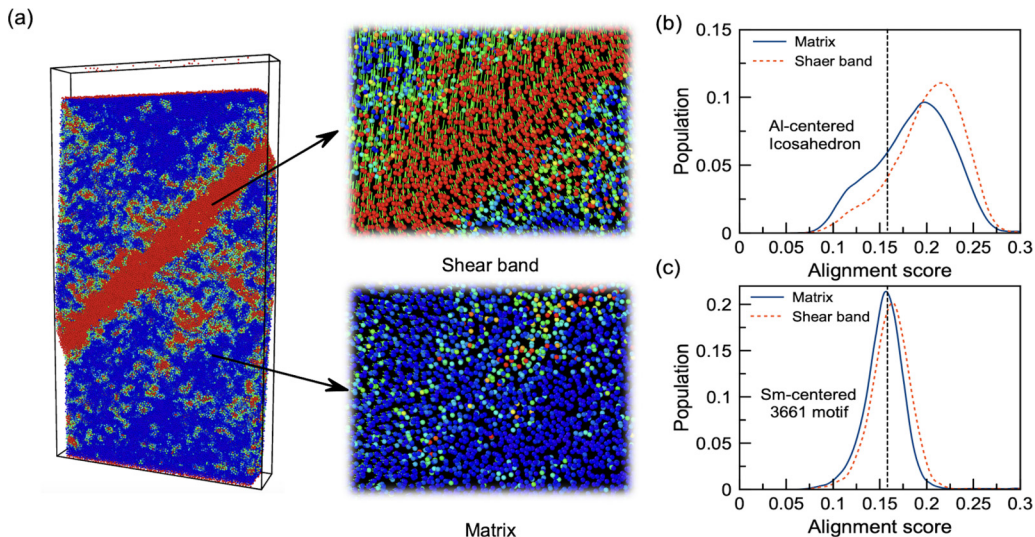


FIG. 7. (a) Local strain and (b), (c) alignment score distribution for the matrix and shear band regions for the simulated $\text{Al}_{90}\text{Sm}_{10}$ model alloys. A cutoff alignment score of 0.16 was used to calculate the fractions of clusters.

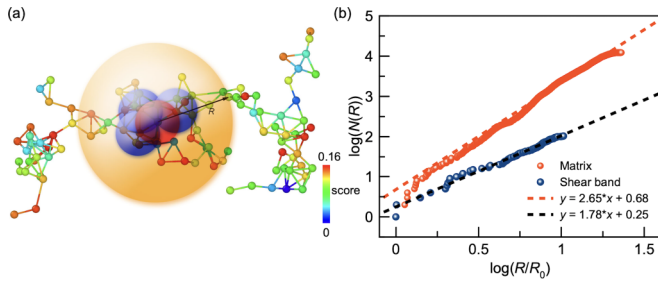


FIG. 9. (a) Schematic of the treelike icosahedral network derived from one root atom. Only the center atoms of the icosahedra are shown and colored according to the alignment score. (b) Double-logarithmic plot of $N(R)$ as a function of R to determine the fractal dimensionality of the icosahedral network in the matrix and the shear band.

connectivity of the icosahedral network by near- T_g annealing. When the shear strain is applied, the change in $\langle N \rangle$ echoes the icosahedral population (see Fig. 6) and the stress-strain curves [see Fig. 1(a)]. When it is near the sudden stress drop, the spatial network begins to collapse, and finally dumps into the narrow band, indicating that the spatial network keeps evolving at different deformation stages. Interestingly, there exists an obvious $\langle N \rangle$ difference for the shear-band and matrix regions of the simulated model alloys. For the as-quenched alloys near the sudden stress drop, $\langle N \rangle$ of the shear-band and matrix regions are 1.81 and 3.40, respectively, indicating a noticeable difference for the atomic packing density.

Furthermore, we examined the “treelike” linkage of the icosahedral network [55]. Figure 9(a), in which only the central atoms of the icosahedra are shown for clarity, helps illustrate how an icosahedral tree derived from a root atom is established. First, a root atom is randomly selected and surrounded by a red sphere with a radius of the cutoff separation $R_0 = 3.5$ Å to enclose all its nearest neighbors. Afterwards, each nearest-neighboring atom is surrounded by a blue sphere of the same size, so that the next level neighbor atoms to the root can be included. This process is repeated and the tree structure is stretched to cover the whole sample. In principle, a different tree can be derived from any seed atom. These convoluted trees serve as the backbone of the glassy structure which is expected to dominate the structural response under external stress.

A direct fractal analysis was applied to describe the fractal patterns of the tree structure. We define $N(R)$ as the number of atoms on the tree within a radius of R from the root atom. A power-law relation for the fractal analysis can be defined as

$$N(R) \propto R^D, \quad (7)$$

where the exponent D is regarded as the fractal dimension. A value of D closer to 3 indicates a more compact packing of icosahedral clusters in space. Figure 9(b) shows $N(R)$ as a function of R for a typical tree established in the matrix and the shear band. At a given R , $N(R)$ is smaller for the

shear band, consistent with the lower density of icosahedral clusters in the shear band [see the inset of Fig. 8(a)]. By employing the double-logarithmic scales for $N(R)$ and R/R_0 , a best fitting line calculated from the least-squares solution gives the fractal dimension D for the shear band and matrix regions to be 2.65 and 1.78, respectively, which are similar to the previous fractal analysis of high pressure or neutron and x-ray diffraction (XRD) experiments [56–58]. The lower value of D again suggests a weakened icosahedral network in the shear band. On the other hand, it is evidenced from Figs. 7–9 that the icosahedral network, albeit weakened, does extend into the shear band. This is in sharp contrast with the Cu-Zr sample, in which the nanocrystalline phase is vanishing in the shear band [see Fig. 5(b)]. This fact explains that while the annealed $\text{Cu}_{64.5}\text{Zr}_{35.5}$ sample shows higher yield strength than $\text{Al}_{90}\text{Sm}_{10}$ due to nanocrystallization, the latter appears to have better ductility due to the remnant structural ordering in the shear band.

IV. CONCLUSION

A comparative structure-property study of $\text{Al}_{90}\text{Sm}_{10}$ and $\text{Cu}_{64.5}\text{Zr}_{35.5}$ alloys in the original and annealed states was performed. For $\text{Al}_{90}\text{Sm}_{10}$, isothermal annealing at a sub- T_g temperature leads to more stable glass structures with lower potential energy and enhanced strength, along with a better-developed network of short-range-order clusters. Under sufficiently large shear stress, the shear strain is largely localized in the shear band, in which the network is weakened but remains clearly discernible. For $\text{Cu}_{64.5}\text{Zr}_{35.5}$ alloys, we observe the primary crystallization of a nanoscale Cu_2Zr Laves phase. Strain localization also occurs under large shear stress, but the crystalline order is almost completely destroyed in the propagating shear band. As a result, the $\text{Cu}_{64.5}\text{Zr}_{35.5}$ alloys display higher yield strength but poorer ductility. It should be noted that it is likely that the phenomena described by these potentials are different from experimental observations. Indeed, as a strong binary glass-forming system, $\text{Cu}_{64.5}\text{Zr}_{35.5}$ is not expected to crystallize at 800 K within a few hundred nanoseconds. Therefore, these two systems are best viewed as two *model* systems that undergo different microstructural evolution in computer simulations, making possible a comparative study of subsequent structural response to external shear stress.

ACKNOWLEDGMENTS

Work conducted at Ames Laboratory was supported by the U.S. Department of Energy, Basic Energy Sciences, Materials Science and Engineering Division, under Contract No. DE-AC02-07CH11358, including a grant of computer time at the National Energy Research Supercomputing Center (NERSC) in Berkeley, California. The GPU-accelerated MD calculations were supported by the Laboratory Directed Research and Development (LDRD) program of Ames Laboratory.

[1] I. Kaban, P. J  v  ri, V. Kokotin, O. Shuleshova, B. Beuneu, K. Saksli, N. Mattern, J. Eckert, and A. L. Greer, *Acta Mater.* **61**, 2509 (2013).

[2] D.   popu, C. Soyarslan, B. Sarac, S. Bargmann, M. Stoica, and J. Eckert, *Acta Mater.* **106**, 199 (2016).

[3] J. Ding, Y.-Q. Cheng, and E. Ma, *Acta Mater.* **69**, 343 (2014).

- [4] A. L. Greer, *Science* **267**, 1947 (1995).
- [5] Z. H. Jin, P. Gumbsch, K. Albe, E. Ma, K. Lu, H. Gleiter, and H. Hahn, *Acta Mater.* **56**, 1126 (2008).
- [6] L. Wan, W. Han, and K. Chen, *Sci. Rep.* **5**, 13441 (2015).
- [7] J. W. Cahn, Y. Mishin, and A. Suzuki, *Acta Mater.* **54**, 4953 (2006).
- [8] A. L. Greer, Y. Q. Cheng, and E. Ma, *Mater. Sci. Eng. R* **74**, 71 (2013).
- [9] M. Lee, C.-M. Lee, K.-R. Lee, E. Ma, and J.-C. Lee, *Acta Mater.* **59**, 159 (2011).
- [10] S. Feng, L. Qi, L. Wang, S. Pan, M. Ma, X. Zhang, G. Li, and R. Liu, *Acta Mater.* **95**, 236 (2015).
- [11] J. Zemp, M. Celino, B. Schönfeld, and J. F. Löffler, *Phys. Rev. B* **90**, 144108 (2014).
- [12] M. P. Allen and D. J. Tildesley, *Computational Simulation of Liquids* (Clarendon Press, Oxford, 1991).
- [13] A. Foroughi, H. Ashuri, R. Tavakoli, M. Stoica, D. Şopu, and J. Eckert, *J. Appl. Phys.* **122**, 215106 (2017).
- [14] M. J. Kramer, H. Mecco, K. W. Dennis, E. Vargonova, R. W. McCallum, and R. E. Napolitano, *J. Non-Cryst. Solids* **353**, 3633 (2007).
- [15] P. Murali and U. Ramamurty, *Acta Mater.* **53**, 1467 (2005).
- [16] J. P. Coleman, F. Meng, K. Tsuchiya, J. Beadsworth, M. LeBlanc, P. K. Liaw, J. T. Uhl, R. L. Weaver, and K. A. Dahmen, *Phys. Rev. B* **96**, 134117 (2017).
- [17] Y. Sun, Y. Zhang, F. Zhang, Z. Ye, Z. Ding, C.-Z. Wang, and K.-M. Ho, *J. Appl. Phys.* **120**, 015901 (2016).
- [18] F. Zhang, M. I. Mendelev, Y. Zhang, C.-Z. Wang, M. J. Kramer, and K.-M. Ho, *Appl. Phys. Lett.* **104**, 016905 (2014).
- [19] J. Zemp, M. Celino, B. Schönfeld, and J. F. Löffler, *Phys. Rev. Lett.* **115**, 165501 (2015).
- [20] R. E. Ryltsev, B. A. Klumov, N. M. Chetchev, and K. Y. Shunyaev, *J. Chem. Phys.* **149**, 164502 (2018).
- [21] M. W. Finnis and J. E. Sinclair, *Philos. Mag. A* **50**, 45 (2006).
- [22] M. I. Mendelev, M. J. Kramer, R. T. Ott, D. J. Sordet, D. Yagodin, and P. Popel, *Philos. Mag.* **89**, 967 (2009).
- [23] M. I. Mendelev, F. Zhang, Z. Ye, Y. Sun, M. C. Nguyen, S. R. Wilson, C. Z. Wang, and K. M. Ho, *Modell. Simul. Mater. Sci. Eng.* **23**, 045013 (2015).
- [24] S. Plimpton, *J. Comput. Phys.* **117**, 1 (1995).
- [25] W. M. Brown, P. Wang, S. J. Plimpton, and A. N. Tharrington, *Comput. Phys. Commun.* **182**, 898 (2011).
- [26] S. Mishra and S. Pal, *J. Non-Cryst. Solids* **500**, 249 (2018).
- [27] G. B. Bokas, L. Zhao, J. H. Perepezko, and I. Szlufarska, *Scr. Mater.* **124**, 99 (2016).
- [28] E. Bitzek, P. Koskinen, F. Gähler, M. Moseler, and P. Gumbsch, *Phys. Rev. Lett.* **97**, 170201 (2006).
- [29] M. L. Falk and J. S. Langer, *Phys. Rev. E* **57**, 7192 (1998).
- [30] X. W. Fang, C. Z. Wang, Y. X. Yao, Z. J. Ding, and K. M. Ho, *Phys. Rev. B* **82**, 184204 (2010).
- [31] Y. Sun, F. Zhang, Z. Ye, Y. Zhang, X. Fang, Z. Ding, C. Z. Wang, M. I. Mendelev, R. T. Ott, M. J. Kramer, and K. M. Ho, *Sci. Rep.* **6**, 23734 (2016).
- [32] H. W. Sheng, W. K. Luo, F. M. Alamgir, J. M. Bai, and E. Ma, *Nature (London)* **439**, 419 (2006).
- [33] A. J. Cao, Y. Q. Cheng, and E. Ma, *Acta Mater.* **57**, 5146 (2009).
- [34] D. Rodney and C. Schuh, *Phys. Rev. Lett.* **102**, 235503 (2009).
- [35] T. Egami, *Prog. Mater. Sci.* **56**, 637 (2011).
- [36] R. Bhowmick, R. Raghavan, K. Chattopadhyay, and U. Ramamurty, *Acta Mater.* **54**, 4221 (2006).
- [37] Z. Han, W. F. Wu, Y. Li, Y. J. Wei, and H. J. Gao, *Acta Mater.* **57**, 1367 (2009).
- [38] J. Q. Wang and J. H. Perepezko, *J. Chem. Phys.* **145**, 211803 (2016).
- [39] M. D. Demetriou, J. S. Harmon, M. Tao, G. Duan, K. Samwer, and W. L. Johnson, *Phys. Rev. Lett.* **97**, 065502 (2006).
- [40] W. L. Johnson, M. D. Demetriou, J. S. Harmon, M. L. Lind, and K. Samwer, *MRS Bull.* **32**, 644 (2011).
- [41] Y. Zhang, F. Zhang, C. Z. Wang, M. I. Mendelev, M. J. Kramer, and K. M. Ho, *Phys. Rev. B* **91**, 064105 (2015).
- [42] Y. Zhang, C. Z. Wang, M. I. Mendelev, F. Zhang, M. J. Kramer, and K. M. Ho, *Phys. Rev. B* **91**, 180201(R) (2015).
- [43] R. E. Ryltsev, B. A. Klumov, N. M. Chetchev, and K. Y. Shunyaev, *J. Chem. Phys.* **145**, 034506 (2016).
- [44] U. R. Pedersen, T. B. Schroder, J. C. Dyre, and P. Harrowell, *Phys. Rev. Lett.* **104**, 105701 (2010).
- [45] E. Kneller, V. Khan, and U. Gorres, *Z. Metallkd.* **77**, 43 (1986).
- [46] D. Arias and J. Abriata, *Bull. Alloy Phase Diagrams* **11**, 452 (1990).
- [47] N. Wang, C. Li, Z. Du, F. Wang, and W. Zhang, *CALPHAD* **30**, 461 (2006).
- [48] G. Ghosh, *Acta Mater.* **55**, 3347 (2007).
- [49] J. Du, B. Wen, R. Melnik, and Y. Kawazoe, *J. Alloys Compd.* **588**, 96 (2014).
- [50] C. Tang and P. Harrowell, *J. Phys.: Condens. Matter* **24**, 245102 (2012).
- [51] F. H. Streitz, J. N. Glosli, and M. V. Patel, *Phys. Rev. Lett.* **96**, 225701 (2006).
- [52] Y. Sun, F. Zhang, Z. Ye, Z. Ding, M. I. Mendelev, M. J. Kramer, C.-Z. Wang, and K.-M. Ho, *Mater. Lett.* **186**, 26 (2017).
- [53] Z. W. Wu, M. Z. Li, W. H. Wang, and K. X. Liu, *Phys. Rev. B* **88**, 054202 (2013).
- [54] M. H. Yang, J. H. Li, and B. X. Liu, *Sci. Rep.* **6**, 29722 (2016).
- [55] M. H. Yang, J. H. Li, and B. X. Liu, *J. Alloys Compd.* **757**, 228 (2018).
- [56] D. Z. Chen, Q. An, Q. S. Zeng, W. L. Mao, W. A. Goddard III, and J. R. Greer, *Science* **349**, 1306 (2015).
- [57] D. Ma, A. D. Stoica, and X. L. Wang, *Nat. Mater.* **8**, 30 (2009).
- [58] Q. Zeng, Y. Kono, Y. Lin, Z. Zeng, J. Wang, S. V. Sinogeikin, C. Park, Y. Meng, W. Yang, H. K. Mao, and W. L. Mao, *Phys. Rev. Lett.* **112**, 185502 (2014).